Active swarms on a sphere

Rastko Sknepnek[1,*] and Silke Henkes[2,†]

[1]*Division of Physics and Division of Computational Biology, University of Dundee, Dundee DD1 5EH, United Kingdom*

[2]*Institute of Complex Systems and Mathematical Biology, Department of Physics,*
University of Aberdeen, Aberdeen AB24 3UE, United Kingdom

We show that coupling to curvature nontrivially affects collective motion in active systems, leading to motion patterns not observed in flat space. Using numerical simulations, we study a model of self-propelled particles with polar alignment and soft repulsion confined to move on the surface of a sphere. We observe a variety of motion patterns with the main hallmarks being *polar vortex* and *circulating band* states arising due to the incompatibility between spherical topology and uniform motion—a consequence of the "hairy ball" theorem. We provide a detailed analysis of density, velocity, pressure, and stress profiles in the circulating band state. In addition, we present analytical results for a simplified model of collective motion on the sphere showing that frustration due to curvature leads to stable elastic distortions storing energy in the band.

I. INTRODUCTION

Active systems, where each particle is equipped with its own source of energy that enables motility, have recently attracted a flurry of interest [1,2]. These systems are characterized by constant input of energy at the individual particle level, rendering them out of equilibrium. Local energy input, many-body effects, and dissipation result in a variety of motion patterns. Examples span multiple length scales ranging from the microscale, e.g., bacterial colonies [3], migration of tissue cells [4], and motion of the cytoskeleton [5] to the macroscale, e.g., fish schools [6], bird flocks [7], and migrating mammals [8]. Important examples on the nonliving side include active nematic fluids [9,10], active colloidal swimmers [11], vibrated granular disks [12], and traffic [13]. Active systems where curvature plays an important role range from biology to physics. On the biological side there are a few prominent examples: curvature and tissue folding are crucial during gastrulation [14], epithelial and endothelial cells move on constantly growing, curved crypts and vili in the gut [15,16], and the mammalian corneal epithelium grows in a steady-state vortex pattern [17]. On the physics side, droplets coated with actively driven microtubule bundles show active nematic patterns [18] that are affected by the underlying curvature of the droplet.

Being far from equilibrium limits the statistical mechanics description of active systems. Instead, one resorts either to hydrodynamic models [2] or to simulations [1]. Despite a large diversity of systems that exhibit active behavior they can be broadly classified based on the particle head-tail symmetry (nematic or apolar), the propulsion symmetry (polar, nematic, or apolar), and momentum conservation (wet) or lack thereof (dry) [2]. A lot of insight was gained by studying toy systems beginning with Vicsek *et al.* [19], who constructed a model of constant velocity self-propelled particles (SPP) that noisily align with their neighbors. In two dimensions, at low noise a state with true long-range order characterized by a finite net velocity appears, in striking contrast to equilibrium systems with continuous order parameter symmetry for which thermal fluctuations destroy long-range order at any finite temperature [20]. Soon after, a hydrodynamic description was constructed using symmetry arguments [21] and later derived microscopically [22,23]. In the Vicsek model, disordered and ordered states are separated by a kinetic phase transition. The nature of this transition has been subject to a long debate [1] with a strong evidence that it is first order [24].

A silent point in the Vicsek model is that particles are pointlike and align instantaneously. The model can be extended to include excluded volume, but its effects remain poorly understood, especially at high densities [25–29]. The phase diagram of active Brownian particles [30] which combines short-range repulsion with angular diffusion has only been characterized recently [31,32]. One distinguishes three phases: at low density and/or small Péclet number (Pe $= v_0/av_r$, a is particle radius and v_r is strength of rotational noise) the system is spatially homogeneous. At higher Péclet numbers, collisional interactions due to volume exclusion reduce the effective velocity, which is proportional to local density [27,33,34]. This leads to a density instability and eventually phase separation via a spinodal decomposition mechanism. The left phase boundary scales with Péclet number, with a suspected lower critical point around Pe $= 10$. The phase-separated region persists at higher density, until at the right spinodal boundary it gives way to a dense liquid phase [31]. At even higher density or lower active driving speeds, the system freezes and forms an active glass or crystal for polydisperse and monodisperse systems, respectively [25,28,29]. It is also known that models with volume exclusion can form stable vortex states in two- and three-dimensional flat space [35,36].

Geometry can play an important role in many systems. One of the most widely studied examples is the structure of the ground states of crystals on surfaces with positive [37] or negative [38] Gaussian curvature. While packing identical particles in plane is straightforward, the ground state is a triangular lattice with each particle having exactly six equidistant nearest neighbors, this is not the case in the presence of curvature. In order to accommodate a nonzero Gaussian curvature one needs to introduce topological defects, i.e. sites
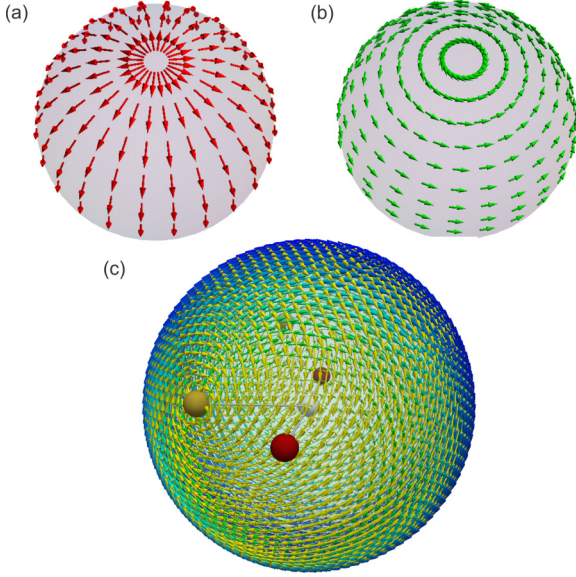
———————
*r.sknepnek@dundee.ac.uk
†shenkes@abdn.ac.uk

FIG. 1. (Color online) Two possible vector field configurations around a +1 topological defect on a sphere: (a) source and (b) whirlpool vortex. (c) Motion pattern of active particles on a sphere. Colored (shaded) arrows indicate velocity vectors, $\mathbf{v}_i$, with the color (shading) proportional to $|\mathbf{v}_i|$. Yellow (gray) arrows represent particles' direction vectors, $\mathbf{n}_i$. We have labeled the positions of the two +1 defects velocity field [red (dark)] and of the director field [golden (light)]. For low activity $\mathbf{v}_i$ and $\mathbf{n}_i$ are not necessarily aligned. Only the whirlpool (b) is consistent with polar active motion on the sphere.

with coordination numbers other than six. This incompatibility between order and curvature leads to geometric frustration. Determining the total number and distribution of the defect in the ground state of a geometrically frustrated system is a complex problem that depends on many details such as global topology of the surface, defect core energy [39], presence and nature of boundaries [40], and so on. Geometry is expected to also affect the flow. For example, it is not possible to have a steady, uniform velocity flow of a fluid on the surface of a sphere. Formally, flow velocity $\mathbf{v}(\mathbf{r})$ is a vector field on S^2 and as a direct consequence of the Poincare's "hairy-ball theorem" [41], there has to be at least one point on S^2 for which $\mathbf{v} = 0$. Vector field configurations that are compatible with the spherical geometry are shown in Figs. 1(a) and 1(b). A similar reasoning should apply to active systems in curved geometries, and thus a flock on a sphere will not be able to take a conformation with all particles traveling at the same speed, like in flat space. Instead, curvature is expected to frustrate dynamics thus leading to complex motion patterns even in the absence of noise.

All SPP models to date have assumed a flat geometry. In this paper, we examine a model of self-propelled particles confined to move on a sphere subject to a realistic alignment rule and white noise. We draw inspiration from recent experiments of Sanchez *et al.* [18] and Keber *et al.* [42]. Our goal here is not to describe those experiments, which requires consideration of hydrodynamic effects but to construct a minimal model that provides clear insight into the interplay between activity and geometry. Our main result is a robust band traveling around the

equator, with a +1 defect at either pole, similar to the ring state found at small vesicle radii in Ref. [42]. The main difference is that due to the polar nature of our model, the ring is rotating, while the ring in Ref. [42] is not.

The paper is organized as follows. In Sec. II we construct a model of active particles confined to move on a sphere. We derive equations of motion for particle positions and orientations subject to the spherical constraint and discuss how those equations are integrated numerically. In Sec. III A we discuss collective motion patterns of this system and in Sec. III B we analyze a steady-state rotating-band pattern unique to the spherical topology. We provide both numerical (Sec. III C) and analytical solutions (Sec. III D) of an effective one-dimensional model for the rotating-band state. In Sec. III F we explore robustness of the rotating-band state with respect to noise and system size. Finally, in Sec. IV we summarize our results and provide an outlook on potential experimental realizations as well as future directions.

II. MODEL

A. Equations of motion

Our model consists of N spherical particles of radius σ confined to the surface of a sphere of radius R [Fig. 2(a)]. Particle velocity $\mathbf{v}_i$ and direction $\mathbf{n}_i$ are constrained to the tangent plane at every point. Each particle is assumed to be actively moving, i.e., it is subject to an internally generated active force $\mathbf{F}_i^{\mathrm{act}}$.

In the overdamped limit the equations of motion are (for a derivation, see Appendix A)

$$\gamma \dot{\mathbf{r}}_i = \mathbf{F}_i^{\mathrm{act}} - (\hat{\mathbf{r}}_i \cdot \mathbf{F}_i^{\mathrm{act}})\mathbf{r}_i + \sum_j \mathbf{F}_{ij} - (\hat{\mathbf{r}}_i \cdot \mathbf{F}_{ij})\mathbf{r}_i, \quad (1)$$

where γ is the friction coefficient and $\mathbf{F}_{ij}$ is the short-range nonactive two-body force. [Explicit forms of $\mathbf{F}_i^{\mathrm{act}}$ and $\mathbf{F}_{ij}$ will be defined below.] If we define the projection operator at a
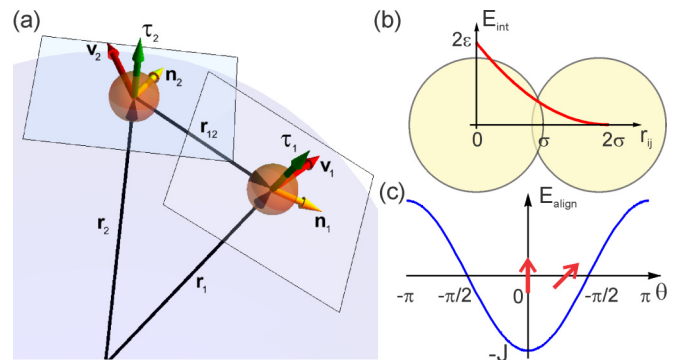

FIG. 2. (Color online) (a) Spherical particles of radius σ are confined to the surface of a sphere of radius R. A unit-length polar direction vector $\mathbf{n}_i$ confined to the tangent plane is assigned to each particle. The velocity vector $\mathbf{v}_i$ is in general not parallel to $\mathbf{n}_i$ but is also confined to the tangent plane; then the torque $\boldsymbol{\tau}_i$ exerted on a particle points along the normal vector at position $\mathbf{r}_i$. The Euclidean distance r_{ij} between particles is computed in the embedding $\mathbb{R}^3$ space. (b) Particles interact via a short-range soft potential, which is finite for any value of r_{ij}. (c) Particle alignment is assumed to follow the *XY* model with ferromagnetic coupling constant J.

point $\mathbf{r}_i$ on to the tangent plane of the sphere acting on a vector $\mathbf{a}$ as $\mathbf{P}_T(\mathbf{r}_i,\mathbf{a}) = \mathbf{a} - (\hat{\mathbf{r}}_i \cdot \mathbf{a})\hat{\mathbf{r}}_i$, the overdamped equations of motion are simply

$$\gamma \dot{\mathbf{r}}_i = \mathbf{P}_T\left(\mathbf{r}_i, \mathbf{F}_i^{\text{act}} + \sum_j \mathbf{F}_{ij}\right). \quad (2)$$

In order to fully describe motion of the particles, we need to also specify dynamics for the internal degree of freedom, i.e., the direction vector $\mathbf{n}_i$. Here we use simple two-dimensional XY-model type dynamics, where a particle aligns explicitly with the surrounding particles within a given radius of interaction. In two dimensions, using first-order dynamics, we have

$$\dot{\phi}_i = -J \sum_j \sin(\phi_i - \phi_j) + \xi_i, \quad (3)$$

where ϕ is the angle of the polar director $\mathbf{n}$ with the x axis, i.e., $\mathbf{n}_i = (\cos\phi_i, \sin\phi_i)$ and the first term on the right-hand side is simply the torque. We have also added a scalar delta-correlated angular noise with distribution $\langle \xi_i(t)\xi_j(t') \rangle = \nu_r \delta_{ij}\delta(t - t')$; ν_r is the noise strength or rotational diffusion constant. On the sphere, it is not possible to define ϕ globally (i.e., uniquely for each tangent plane), so we need to write the equation in terms of $\mathbf{n}_i$ directly. In the plane, the right-hand side of Eq. (3) can be written as a curl projected along the $\mathbf{e}_z$ axis orthogonal to the xy plane to obtain its magnitude:

$$\dot{\phi}_i = -J \left(\sum_j \mathbf{n}_i \times \mathbf{n}_j\right) \cdot \mathbf{e}_z + \xi_i. \quad (4)$$

If we define the normal projection of a vector on the unit normal to the tangent plane as $P_N(\hat{\mathbf{r}}_i,\mathbf{a}) = (\mathbf{a} \cdot \hat{\mathbf{r}}_i)$, the deterministic part of the right-hand side of Eq. (4) is simply $P_N(\hat{\mathbf{r}}_i, -J \sum_j \mathbf{n}_i \times \mathbf{n}_j)$. The derivative of a unit vector is an angular rotation, and we have $\frac{d\mathbf{n}_i}{dt} = \dot{\phi}_i(\hat{\mathbf{r}}_i \times \mathbf{n}_i)$, that is, the time derivative is orthogonal to both the axis of rotation and the vector itself. Then the XY-like angular dynamics on the sphere is given by:

$$\frac{d\mathbf{n}_i}{dt} = \left[P_N\left(\hat{\mathbf{r}}_i, -J \sum_j \mathbf{n}_i \times \mathbf{n}_j\right) + \xi_i \right] (\hat{\mathbf{r}}_i \times \mathbf{n}_i). \quad (5)$$

We note that the fully vectorial approach is as well beneficial from the point of view of numerical simulations as it is straightforward to generalize to an arbitrary surface, unlike working with local parametrizations, which often have singular points (e.g., for $\theta = 0$) and can be costly to compute numerically.

B. Integrating the equations of motion

In this study we assume that the active force has a simple form, $\mathbf{F}_i^{\text{act}} = v_0 \mathbf{n}_i$, with magnitude v_0 pointing along $\mathbf{n}_i$, and define the mobility $\mu = \gamma^{-1}$, leading to the following equation of motion:

$$\dot{\mathbf{r}}_i = \mathbf{P}_T\left(\mathbf{r}_i, v_0 \mathbf{n}_i + \mu \sum_j \mathbf{F}_{ij}\right). \quad (6)$$

The interaction force $\mathbf{F}_{ij}$ is modeled as a short-range repulsion between spheres of radius σ, $\mathbf{F}_{ij} = -k(2\sigma - r_{ij})\frac{\mathbf{r}_j - \mathbf{r}_i}{r_{ij}}$ for $r_{ij} < 2\sigma$ and $\mathbf{F}_{ij} = 0$ otherwise, with k being the elastic constant; r_{ij} is the Euclidean distance computed in $\mathbb{R}^3$. For the alignment dynamics we consider only the "ferromagnetic" case where the coupling constant $J > 0$ and the j-sum in Eq. (5) is carried over all neighbors within a 2.4σ cutoff radius, i.e., the first shell of neighbors. Particle orientation is subject to delta-correlated noise ξ_i acting in the tangent plane with rotational diffusion constant ν_r.

An important feature of our model is the separate dynamics of $\mathbf{n}_i$ and $\mathbf{v}_i$ [4]. In the absence of interactions, $\mathbf{n}_i$ and $\mathbf{v}_i$ will eventually align. The interparticle forces, however, allow for permanent deviations of $\mathbf{v}_i$ from $\mathbf{n}_i$, a key mode for active elastic energy storage [25]. The coupling constant J sets an alignment time scale, $\tau_{\text{al}} \approx 1/J$. Similarly, the collision time scale is set by k as $\tau_{\text{col}} \approx 1/\mu k\Delta$, where Δ is the maximum overlap with respect to σ. In the following, length is measured in units of σ, energy in units of $k\sigma^2$, time in units of $\tau = 1/\mu k$, velocity in units of $\sigma/\tau \equiv \mu k\sigma$, and ν_r in units of τ^{-1}. Finally, Eqs. (6) and (5) were integrated numerically. Instead of choosing a curvilinear parametrization of the sphere we kept the equations in vector form and imposed constraints after each step. Each time step has two stages: (1) unconstrained move according to Eq. (6) and (2) projection of the position onto the sphere and its velocity and orientation onto the tangent plane at the new position. Similarly, torques were projected onto the surface normal at $\mathbf{r}_i$ and, finally, $\mathbf{n}_i$ was rotated by a random angle around the same normal.

All simulations except Sec. III F were performed with $N \approx 3 \times 10^3$ particles at packing fraction $\phi = 1$ (defined as the ratio of the area occupied by all particles to the total area of the sphere, i.e., $\phi = N\pi\sigma^2/4\pi R^2$), resulting in $R \approx 28.2\sigma$. For comparison, we performed a series of simulations in the plane with the same N and ϕ by imposing periodic boundary conditions onto a square simulation box of size $L = 100\sigma$. In all cases, the equations of motion were integrated for a total of $10^4\tau$ with time step $\delta t = 10^{-3}\tau$ using a standard Euler-Maruyama method. Initially, particles were placed at random on the sphere, then initial large overlaps were removed by using a simple energy relaxation scheme.

III. RESULTS AND THEORY

A. Collective dynamics

In Fig. 3 we show snapshots of typical motion patterns for $v_0 = 0.03\sigma/\tau$, $0.1\sigma/\tau$, and $1.0\sigma/\tau$ (we also include movies in the Supplemental Material [43]). Here we focus on the low-noise ($\nu_r = 0.002\tau^{-1}$) and large-packing-fraction ($\phi = 1$) regime. Effects of a stronger noise will be addressed in Sec. III F. For low v_0 one observes a polar vortex pattern [Fig. 3(a)]. In this state, spherical symmetry is spontaneously broken and two vortices form at opposite poles [see Fig. 1(b)]. The entire flock rotates around the axis passing through those poles. This circulating band has neither sources nor sinks, as required for a particle conserving fluid, and is consistent only with the pattern in Fig. 1(b). Linear velocity within the flock is not uniform, gradually decreasing from $\approx v_0$ at the equator to zero toward the poles. In general, $\mathbf{n}_i$ is not aligned with $\mathbf{v}_i$ and

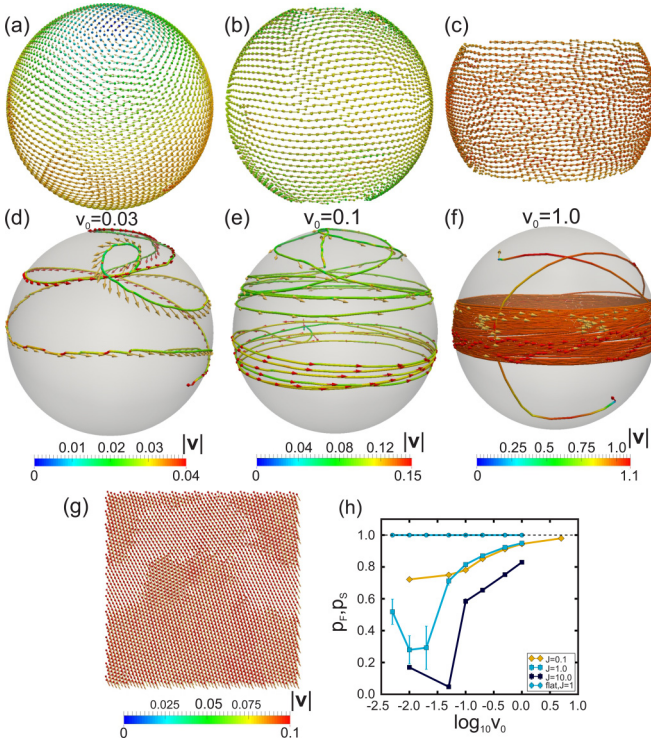FIG. 3. (Color online) Steady-state configurations at $t = 10^4\tau$ for (a) $v_0 = 0.03\sigma/\tau$, (b) $v_0 = 0.1\sigma/\tau$, and (c) $v_0 = 1\sigma/\tau$, with $J = 1\tau^{-1}$ and $\nu_r = 0.002\tau^{-1}$. The length and color (shading) of velocity vectors reflect the magnitude of $|\mathbf{v}_i|$. Thinner yellow (bright) vectors indicate the directions of the orientation vectors $\mathbf{n}_i$. Panels (d), (e), and (f) show trajectories of two randomly selected particles colored according to $|\mathbf{v}_i|$; vectors along the trajectory indicate $\mathbf{n}_i$ at these positions. (g) is a snapshot of the $v_0 = 0.1\sigma/\tau$ periodic flat system of size $L = 100\sigma$; here $\mathbf{v}_i$ [red (dark)] is uniform and completely aligned with $\mathbf{n}_i$ [yellow (bright)]. Panel (h) shows the order parameters for the flat (p_F) and spherical (p_S) systems as a function of v_0 for a range of values of J. Please see the Supplemental Material for movies of the band and flat states [43].

forms separate vortices [gray (light) arrows in Fig. 1(c)]. The motion is heavily frustrated with short-lived localized velocity spikes and rearrangements [longer arrows in Fig. 1(c)], leading to substantial mixing as can be seen by tracking individual particle trajectories [Fig. 3(d)]. As v_0 increases, the system develops "bald" spots at the poles. Particles are compressed toward the equator and the flock takes the configuration of a spherical belt. $\mathbf{n}_i$ and $\mathbf{v}_i$ are more closely aligned and there are fewer jumps in velocity. Finally, as v_0 is increased to $1.0\sigma/\tau$, the flock is squeezed further toward the equator. The velocity distribution within the flock is nearly uniform and $\mathbf{n}_i$ and $\mathbf{v}_i$ are almost aligned. Particle trajectories are very regular [Fig. 3(f)].

Local reductions of velocity due to volume exclusion and decoupling of $\mathbf{n}_i$ and $\mathbf{v}_i$ lead to active phase separation [26,27], an effect distinct from the banding observed here: We have examined the flat-space counterpart of our system in the same range of values of v_0 and J as in the spherical case. It remains in the homogeneous phase (Fig. 3(g) and Supplemental Material movie [43]). Using a Vicsek order parameter $p_F =$

$\frac{1}{Nv_0}\left|\sum_i \mathbf{v}_i\right|$, we show that this flat system is also consistently in the polar phase, with $p_F \approx 1$ independent of v_0 [Fig. 3(h)]. In the spherical case, we measure alignment on the surface of the sphere. We define $p_S = \frac{1}{NRv_0}|\sum_i \mathbf{r}_i \times \mathbf{v}_i|$, $p_S \to 1$ for a circulating ring moving at v_0. p_S transitions from a low value for small v_0 to near perfect alignment at larger v_0 [Fig. 3(h)]. The dip in p_S at intermediate v_0 is potentially indicative of curvature-influenced active phase separation. Conditions that lead to such effects will be addressed elsewhere [44]. These results shows that the transition to the polar vortex and a moving band is a purely curvature-driven effect, with no equivalent in the planar model.

The phenomenon is similar to the ring structures found in the plane [35] and in three dimensions [36], with the important difference that in here it occurs in the absence of attraction. Active contractile elements have also been studied in a continuum model on a cylinder and show banding [45]. We note that without the self-avoidance (i.e., at $k = 0$), our model reduces to a continuum Vicsek model. In contrast to the polar ordered state observed on the plane, on the sphere after a long relaxation period the entire flock collapses into a ring spanning one of the great circles. The effect again differs from the density banding close to the Vicsek transition [46] since it occurs deep inside the polar regime.

We focus only on the high-velocity regime with a developed band. The system spontaneously breaks spherical symmetry along an arbitrary axis. Therefore, in order to produce the angular profiles (Fig. 4), for each snapshot we first determined the direction of the total angular velocity and then performed a global rotation that aligned it with the z axis in $\mathbb{R}^3$. In Figs. 4(a) and 4(b) we present such profiles for the density and pressure in the established band for $J = 1\tau^{-1}$ and a range of v_0. The density has been normalized to that of a uniformly covered sphere, and we measure pressure by computing the trace of the local *force moment tensor*, $\hat{\Sigma}_i = \sum_j \mathbf{r}_{ij}\mathbf{F}_{ij}$, with units of energy (see Sec. III E). The band has a relatively complex structure. For example, the discrete particles lead to a distinct layering pattern in the density profiles. Similarly, a change of slope in the pressure profiles stems from double overlaps among very compressed particles, though, overall, the band narrows and the pressure increases with growing v_0. The influence of J is at first counterintuitive (Fig. 4, insets): The *lower* values of J where the alignment is weaker lead to more pronounced banding.
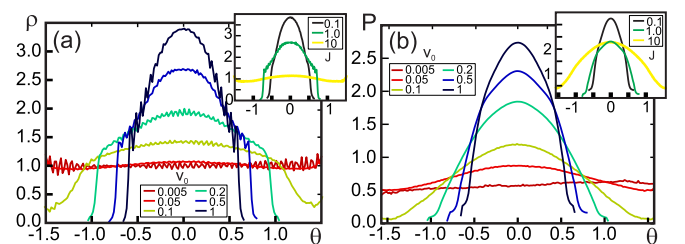

FIG. 4. (Color online) (a) Density profiles for increasing v_0 at $J = 1\tau^{-1}$. Inset: Density profiles as a function of J for $v_0 = 0.5\sigma/\tau$. (b) Pressure profiles (virial part), same parameters as in (a). Curves are ordered from flat to peaked with increasing v_0 and from peaked to flat with increasing J.
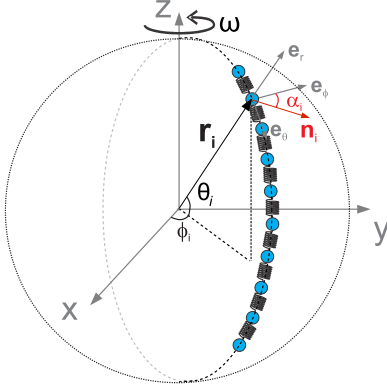
FIG. 5. (Color online) Linked spring chain model for a slice of the rotating-band solution. We assume that the band is moving with a constant angular velocity $\omega = v_0/R$, i.e., the velocity of each particle is locally aligned with $\mathbf{e}_\phi$. In this case, we can extract a "column" of particles along the polar direction, leading to the effective model for the band state. Particles are assumed to be connected to their nearest neighbors via harmonic springs of stiffness k. Each particle is subject to a force in the $\mathbf{e}_\theta$ direction resulting from the motion on the small circles on the sphere. In general, particle orientation $\mathbf{n}_i$ is not aligned with the velocity $\mathbf{v}_i$ but instead deviates from it by an angle α_i.

B. Steady-state rotating solution

In the simulations, we also observe a steady-state rotating solution (the rotating-band state) where particles cluster symmetrically around the equator and the entire flock performs a solidlike rotation with angular velocity ω around an axis through the poles.

To understand this, we use a simplified one-dimensional model to analyze the active mechanics of an already-formed band. We consider a one-particle wide "orange" slice cut out of the sphere in the polar direction as shown in Fig. 5. The particles in the slice all move in the same tangential direction, $\mathbf{e}_\phi$, with constant angular velocity $\omega = v_0/R$, i.e., with decreasing speed toward the poles. In local spherical coordinates the particle position is $\mathbf{r}_i = R(\cos\theta_i \cos\phi_i, \cos\theta_i \sin\phi_i, \sin\theta_i)$, where the z axis is aligned with the axis of rotation, θ_i is the angle from the xy plane along a meridian, and ϕ_i is the azimuthal angle. Since the active force $\mathbf{F}_i^{act} = v_0 \mathbf{n}_i$ is always in the tangent plane, we can write $\mathbf{n}_i = \cos\alpha_i \mathbf{e}_\phi - \sin\alpha_i \mathbf{e}_\theta$. Here α_i is the (signed) angle between the polar direction and the band velocity parallel to the equator. We derive a simple relation between rotation speed and active forces by projecting Eq. (6) onto the $\mathbf{e}_\phi$ direction. We have $\dot{\mathbf{r}}_i = R\omega \cos\theta_i \mathbf{e}_\phi$, leading to:

$$\cos\alpha_i = \frac{R\omega}{v_0} \cos\theta_i. \tag{7}$$

In this simplest case, the solution is radially symmetric. It corresponds to a symmetric vector field pointing inwards to both sides of the equator [visible in Fig. 3(c)]. In Fig. 6(b), we show simulation results for α versus θ profiles for three different values of the alignment parameter J. All profiles are linear and nearly independent of v_0, with a slope that depends only on J. Since α_i is also the angle between the polar direction and the velocity, it now makes sense that α *reduces* for large values of J. With s the slope of the graph, we have $\alpha = s\theta$,
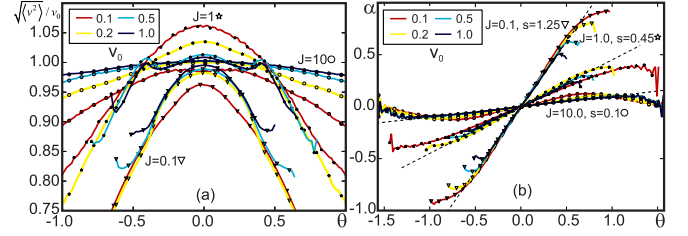

FIG. 6. (Color online) (a) Velocity profiles ($\sqrt{\langle v^2 \rangle}/v_0$) for increasing v_0 and three values of J. From peaked to flat: $J = 0.1\tau^{-1}, J = 1\tau^{-1}$ and $J = 10\tau^{-1}$. (b) Simulation results for α, the angle with the velocity direction, as a function of θ, for different v_0 (legend) and J. From steep to shallow: $J = 0.1\tau^{-1}$, with fitted $s = 1.25$; $J = 1\tau^{-1}$ with $s = 0.45$; and $J = 10\tau^{-1}$ with $s = 0.15$.

with $s \approx 1.25, 0.45$, and 0.1 for $J = 0.1\tau^{-1}, 1\tau^{-1}$, and $10\tau^{-1}$, respectively [we use $s = 0.55$ for the fits of the $J = 1$ profiles in Figs. 7(a) and 7(c)].

In Fig. 6(a) we show the velocity magnitude profiles for three values of J and a range of v_0. In all cases, velocities reach near or above v_0 at the center of the band and then reduce toward the edges but are more complex than the simple parabolic profile predicted by Eq. (7). However, they retain sufficiently close similarity to a parabolic profile in the region where the density is nonzero for the approximation $\omega = v_0/R$ to remain valid.

In order to further analyze the single-slice model we suppose that the chain consists of N_p particles pole to pole. We chose N_p such that $p\sigma^2 \approx 0.5k$ in the absence of activity, consistent with the low velocity and flat value of the pressure [see Fig. 4(b)]. Assuming overlapping particles, the force an adjacent particle j exerts on particle i in the chain is given by $\mathbf{F}_{ij} = -k\hat{\mathbf{r}}_{ij}(2\sigma - |\mathbf{r}_j - \mathbf{r}_i|)$. If we expand around θ_i, we can approximate $\mathbf{r}_j - \mathbf{r}_i = -R(\theta_j - \theta_i)\hat{\mathbf{e}}_\theta$. To first order, interparticle forces are along $\hat{\mathbf{e}}_\theta$, and the forces acting on particle i from its neighbors $i-1$ and $i+1$ are $F_{i,i-1} = k[2\sigma - R(\theta_i - \theta_{i-1})]$ and $F_{i,i+1} = -k[2\sigma - R(\theta_{i+1} - \theta_i)]$,
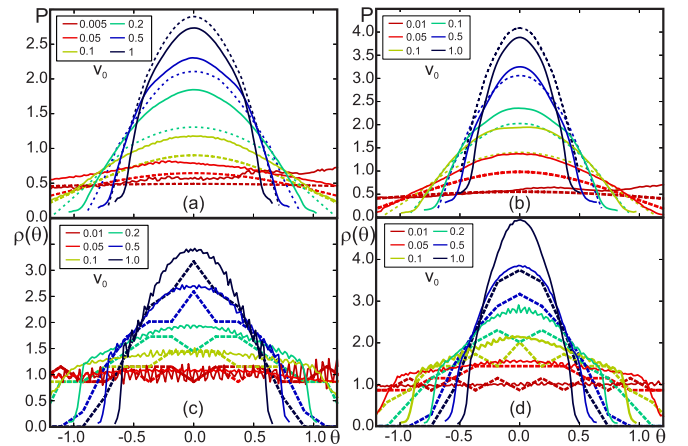

FIG. 7. (Color online) Simulation results (solid) and full chain calculation (dashed) compared to each other, for $J = 1\tau^{-1}$ and $s = 0.55$ (a) and (c) and $J = 0.1\tau^{-1}$ and $s = 1.25$ (b) and (d). Top row: pressure, and bottom row: density. Curves are ordered from flat to peaked with increasing v_0, for both pressure and density, and also simulation and calculation results.

respectively. Finally, we can write the set of equations of motion along the chain:

$$v_0 \sin \alpha_1 = -\mu k \left[2\sigma - R(\theta_2 - \theta_1) \right]$$

$$v_0 \sin \alpha_i = -\mu k R(\theta_i - \theta_{i-1}) + \mu k R(\theta_{i+1} - \theta_i) \quad (8)$$

$$v_0 \sin \alpha_{N_p} = \mu k [2\sigma - R(\theta_{N_p} - \theta_{N_p-1})].$$

We solve these equations using two approaches.

C. Numerical energy minimization approach

First, we treat Eqs. (8) as Euler-Lagrange equations of an effective energy functional. Formally, even though our physical system conserves neither energy nor momentum, if we assume $\alpha = s\theta$, the active force components in Eq. (8) derive from an effective potential $V_{\text{act}}^i = v_0 \cos(s\theta_i)$ which can be added to the interparticle repulsive term $V_{\text{rep}}^i = \frac{kR}{2} \sum_{j \in \mathcal{N}} (\theta_j - \theta_i)^2$. Then setting the gradients of $V^i = V_{\text{act}}^i + V_{\text{rep}}^i$ to zero is equivalent to Eq. (8). We then minimize the potential by using the standard L-BFGS-B conjugate gradient method [47] including boundary constraints and compute strain and pressure from the numerically evaluated displacements.

The alignment parameter J only appears through its influence on the parameter s, with s decreasing for larger alignment strengths. Then the main remaining dynamical parameter is just v_0. Another important quantity is the dimensionless curvature $\kappa (=2\sigma/R = 0.0708982)$. An important point is to determine the correct initial state for the chain. Because of the unit packing fraction ($\phi = 1$), one might expect that just touching spheres with no prestress are the correct initial state. However, it is known that $\phi = 1$ corresponds to the jammed or crystalline region of phase space, where soft particles interpenetrate [48]. In Fig. 8(b), we show the mean pressure (or, to be precise, the trace of the force-moment tensor) in the spherical system as a function of v_0 and compare it to the pressure in an equivalent flat system. For the flat system, the pressure is very close to constant, indicating no strain-inducing distortions due to activity, consistent with the observed collective block translation in these cases. The constant value $p_0 = 0.5k/\sigma^2$ stems purely from the overlaps of the particles due to the initial packing. If we assume $\bar{z} = 6$ neighbors
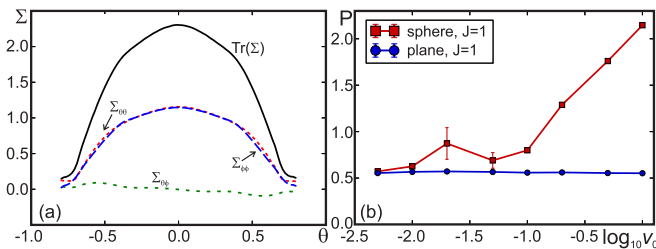
on average, we can estimate an initial overlap of roughly $\delta_0 = 0.1\sigma$. To make a quantitative comparison between the one-dimensional chain model and the simulation, we need the same starting value of p_0. Therefore we prepare the chain with initial overlaps of $\delta = 0.25\sigma$. For the sphere radius used in the simulation, this is equivalent of a chain with $N_p = 59$. In order to be able to reliably use a one-dimensional model for our two-dimensional system, we need to show that the local stresses are homogeneous [see Fig. 8(a) and Sec. III D].

When comparing simple chain "energy" minimization results to the simulations, it becomes apparent that it dramatically underestimates the pressure in the center of the band. This points to a larger effective stiffness constant $\bar{k} > k$ in the center. A straightforward explanation is double or even multiple overlaps of particles, i.e., next-nearest neighbor and further interactions. We have confirmed their existence in the simulated bands and incorporate them into the chain minimization procedure by counting *all* neighbors in the repulsive term $V_{\text{rep}}^i = \frac{kR}{2} \sum_{j \in \mathcal{N}} (\theta_j - \theta_i)^2$. Due to the initial compressed state, we also add a constraint $0 \leqslant \theta_i \leqslant \pi$ to the L-BFGS-B minimization routine. Finally, with this amount of detail, the continuum formulations $p = \bar{k} u_s$ and $\rho = 1 + u_s$ lose their meaning and we directly compute the pressure via the force moment tensor and the density through a histogram. Figure 7 shows the numerical stress and density profiles for $J = 0.1\tau^{-1}$ and $J = 1\tau^{-1}$, overlaid with the full chain minimization results. We have used $s = 1.25$ for $J = 0.1\tau^{-1}$ as fitted but had to adjust $s = 0.55$ for $J = 1\tau^{-1}$, indicating that the chain model approximations work better for a narrowly peaked band. The model provides a good quantitative fit for both sets of simulation (Fig. 7).

For large values of J ($J \approx 10\tau^{-1}$), the peaked density profile is slow to develop, and the pressure profile remains very broad at all values of v_0. We were not able to satisfactorily fit them with any value of s. At low v_0 and large values of J, we reach an intermediate phase where the recently discovered density instability in repulsive self-propelled particles (see, e.g., Ref. [33]) influences the behavior, and we do not obtain a symmetric band but rather a circulating patch [44]. This is also visible in the order parameter graph, Fig. 3(h), where there is a consistent dip in the order parameter at intermediate values of v_0 for the higher values of J.

D. Continuum model

The second approach to solving Eqs. (8) is based on taking the continuum limit and is less straightforward but a bit more physically insightful. If our system is large, i.e., if $\kappa = 2\sigma/R \ll 1$, where κ is the dimensionless curvature of the sphere, the angular differences can be written in differential form. Let the u_i be the displacement of the particle i from its rest position, i.e.,

$$\theta_i = \theta_i^0 + u_i, \quad (9)$$

with $\theta_i^0 = \frac{2\sigma i}{R} - \frac{\sigma N}{R}$.

This transformation needs to be performed carefully, and we can use either an absolute reference frame or the coordinates of the particles themselves, corresponding to Eulerian and Lagrangian pictures, respectively. Details of the calculation are given in Appendix B. In the Lagrangian reference frame,

FIG. 8. (Color online) (a) Averaged profiles of the components of the force moment tensor in the local frame $\mathbf{e}_r$, $\mathbf{e}_\theta$, $\mathbf{e}_\phi$, for $J = 1\tau^{-1}$ and $v_0 = 1\sigma/\tau$. The stress tensor is close to isotropic on the sphere, with $\Sigma_{\theta\theta} \approx \Sigma_{\phi\phi}$, the off-diagonal components are much smaller. Due to the projection, all components involving $\mathbf{e}_r$ are zero. (b) Mean pressure for the spherical and flat cases as a function of v_0. The active part of the pressure is only significant compared to the overlap part of the pressure $p_0 \approx 0.5$ for the spherical case; in other words activity does not induce energy-storing distortions in the flat case.

the equation for the displacement u is

$$\frac{d^2u}{d\theta_0^2} = \alpha \sin(s\theta_0 + su), \tag{10}$$

with boundary conditions

$$\frac{du}{d\theta_0}\bigg|_{\mp\theta_{m,0}} = \pm\beta \sin(s\theta_0 + su). \tag{11}$$

In the Eulerian reference frame, the right-hand side term is simpler; however, additional derivatives arise on the left-hand side:

$$\left(1 + \frac{du}{d\vartheta}\right)^2 \frac{d^2u}{d\vartheta^2} = \alpha \sin(s\vartheta), \tag{12}$$

with boundary conditions

$$\left(1 + \frac{du}{d\vartheta}\right)\frac{du}{d\vartheta}\bigg|_{\mp\vartheta_m} = \pm\beta \sin(s\vartheta). \tag{13}$$

Here $\alpha = \frac{1}{R}[\frac{R}{2\sigma}]^2 \frac{v_0}{\mu k}$ and $\beta = \frac{v_0}{2\sigma\mu k}$, and the boundary conditions have to be taken at the original position of the chain edges $\theta_{m,0}$ in the Lagrangian case but at the final position ϑ_m for the Eulerian equations. Note that the two approaches are strictly equivalent, as can be seen by applying a change of variable $\theta_0 = \vartheta - u$ and $d\theta_0 = (1 + \frac{du}{d\vartheta})d\vartheta$ to the Lagrangian equations.

We briefly summarize the results derived in Appendix B. The Eulerian solution at the zeroth order is

$$u(\vartheta) = -\alpha/s^2 \sin s\vartheta + (\alpha/s \cos s\vartheta_m - \beta \sin s\vartheta_m)\vartheta, \tag{14}$$

where we have only an implicit equation for the band edge ϑ_m [Eq. (B14)]. In the Lagrangian case, at the zeroth level the solution is simpler:

$$u(\theta_0) = -\frac{\alpha}{s^2}\sin s\theta_0 + \left[\frac{\alpha}{s}\cos\frac{s\pi}{2} - \beta\sin\frac{s\pi}{2}\right]\theta_0; \tag{15}$$

however, to compare to simulation results, all expressions have to be evaluated at the new positions $\vartheta = \theta_0 + u(\theta_0)$.

The Eulerian strain is given by

$$u_s^E(\vartheta) = \frac{du}{d\vartheta} - \frac{1}{2}\frac{du}{d\vartheta}\frac{du}{d\vartheta} \approx -\frac{1}{2R}\left[\frac{R}{\sigma}\right]^2$$
$$\times \frac{v_0}{\mu k}\left[\frac{1}{s}(\cos s\vartheta - \cos s\vartheta_m) + \frac{2\sigma}{R}\sin s\vartheta_m\right], \tag{16}$$

where we have only kept the first-order strain term $\frac{du}{d\vartheta}$ in the second equation. In Lagrangian coordinates, at the first order, we have the exact same expression, except using θ_0 instead of ϑ and $\pi/2$ instead of θ_m.

E. Predicting strain, pressure, and density profiles

We can estimate the pressure profile within the dense phase by noting that the interparticle forces are related to the derivative of the displacement profile:

$$F_{i,i+1} = -k[2\sigma - R(\theta_{i+1} - \theta_i)] = 2k\sigma\frac{du}{d\theta}. \tag{17}$$

This is assuming that all the $F_{i,i+1} = 0$ before any displacements were applied, or, in other words, we have no prestress

in the system. The interaction part of the stress tensor at the local scale is given by

$$\hat{\sigma}_i = \frac{1}{A_i}\sum_j \mathbf{r}_{ij} \otimes \mathbf{F}_{ij}, \tag{18}$$

where the $\mathbf{r}_{ij}$ reach from the center of each particle to the contact and A_i is the part of an area tessellation (e.g., Voronoi diagrams) belonging to particle i [49,50]. Ignoring second-order contributions in u, we estimate $r_{ij} \approx \sigma$ and $A_i \approx 4\sigma^2$. If each particle has four contacts, and horizontal forces equal vertical forces (i.e., the stress field is isotropic), the pressure is given by $p_i = \mathrm{Tr}\hat{\sigma}_i = 2k\frac{du}{d\vartheta}$ (note the units of force divided by length, or stiffness, appropriate to two dimensions). This is really just a microscopic derivation of the stress-strain relation, and we should write $p = \bar{k}u_s(\vartheta)$, with a possibly effective stiffness constant $\bar{k}$.

To test our assumption of an isotropic stress field, we analyzed the components of the force moment tensor in the local frame $\mathbf{e}_r$, $\mathbf{e}_\theta$, $\mathbf{e}_\phi$ ($\hat{\Sigma}_i = A_i\hat{\sigma}_i$ is the additive version of the stress tensor, with units of energy). Here the components $\Sigma_{\theta\theta}$ and $\Sigma_{\phi\phi}$ correspond to stresses along a meridian and perpendicular to it, respectively, and the components $\Sigma_{\theta\phi}$ are the off-diagonal components. For an isotropic stress tensor $\Sigma_{\theta\theta} \approx \Sigma_{\phi\phi}$, the off-diagonal components are much smaller and, due to the projection, all of the components involving $\mathbf{e}_r$ are zero. Figure 8(a) shows that in a developed band, these approximations hold to a very high degree.

Then the predicted pressure profile for $|\vartheta| < \vartheta_m$ is (again, neglecting the second-order contributions to the strain)

$$p(\vartheta) = -\frac{v_0 R}{2\mu\sigma^2}\left[\frac{1}{s}(\cos s\vartheta + \cos s\vartheta_m) - \frac{2\sigma}{R}\sin s\vartheta_m\right], \tag{19}$$

with an equivalent expression for the Lagrangian pressure profile.

Finally, we can also compute the angular density profile: We define the local density to be $\rho = 1$ when particles are just touching (i.e., the unperturbed chain). Then, assuming again isotropic compression like for the pressure profile above, $\rho \approx 1 + |\frac{du}{d\theta}|$, or, more precisely, using the strain $\rho(\vartheta) = 1 - u_s(\vartheta)$. The density profile is $\rho = 0$ for $|\vartheta| > \vartheta_m$ and to first order we have

$$\rho(\vartheta) = 1 - \frac{1}{2R}\left[\frac{R}{2\sigma}\right]^2\frac{v_0}{\mu k}$$
$$\times \left[\frac{1}{s}(\cos s\vartheta - \cos s\vartheta_m) + \frac{2\sigma}{R}\sin s\vartheta_m\right], \tag{20}$$

within the band and $\rho = 0$ otherwise. Interestingly, unlike the pressure, the density depends on k and does not seem to be universal. Again, there is a similar equivalent equation for the Lagrangian density prediction.

Figures 9(a) and 9(b) show the analytical predictions for the pressure profiles (plotting $-p$) using the *full* Eulerian and Lagrangian strain tensors, evaluated at the simulation parameters for R, σ, and v_0 and using MATHEMATICA to numerically solve the implicit equation for ϑ_m. We have also used $s = 1$ and ignored any prestress contributions. While the profiles agree with each other at low v_0, there are considerable
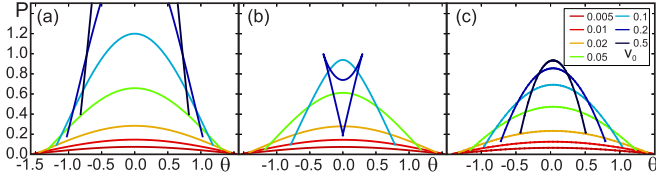
FIG. 9. (Color online) Comparing the analytical solution to energy minimization. (a) Analytical zeroth-order Eulerian solution using the full Eulerian strain tensor. (b) Analytical zeroth-order Lagrangian solution, starting from the full Lagrangian strain tensor. (c) Predicted pressure of the single-overlap chain with $N = 44$ (just touching) particles. Note the good agreement at low values of v_0. The remaining parameters are $s = 1$, $p_0 = 0$, R and σ as in the simulation. Curves are ordered from flat to peaked with increasing v_0.

differences at higher v_0; the Lagrangian solution also stops being single valued due to $u \gg \theta_0$ in evaluating ϑ.

In summary, the form of the strain u_s, to leading order in either the Lagrangian or Eulerian picture, is

$$u_s(\theta) = -\frac{v_0}{\sigma \mu k}\left[\frac{\cos(s\theta) - \cos(s\theta_m)}{\kappa s} + \sin(s\theta_m)\right], \quad (21)$$

which we use to extract density and pressure profiles. Here θ_m is the location of the band edge, itself a model output. Assuming a homogeneous system, the pressure (virial part) is given by the stress-strain relation $p = \bar{k}u_s$ ($\bar{k}$ is an effective stiffness) and density $\rho/\rho_0 \approx 1 - u_s$, where ρ_0 is the initial density. $\kappa = 2\sigma/R$ is the dimensionless curvature of the sphere. Negative strain indicates increased density and inward pressure, consistent with a compressed band. The inward pressure at the edges, $p = -\frac{v_0}{\sigma \mu}\sin(s\theta_m)$, is equal and opposite to the active force per unit length, $\frac{v_0}{\sigma \mu}\sin\alpha$, due to the self-propulsion, that is, pressure balance reminiscent of active phase separation [26,27] and a first-order phase transition. From our analysis, four important dimensionless parameters emerge: the reverse alignment strength s, the underlying curvature $\kappa \approx 0.07$, the active pressure $v_0/\sigma \mu$, and the density through θ_m.
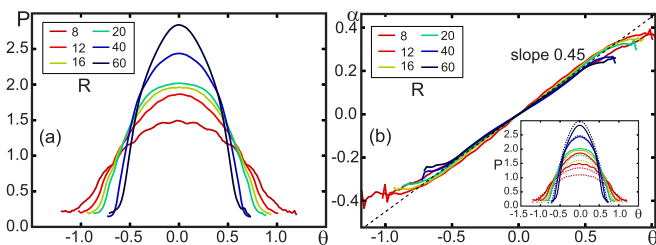

FIG. 10. (Color online) Scaling of the band properties with radius R. Left: Pressure profiles over two decades in system size, from $R = 8\sigma$ to $R = 60\sigma$, for $v_0 = 0.5\sigma/\tau$, $\phi = 1$ and $J = 1\tau^{-1}$. Right: The $\alpha - \theta$ profile is independent of system size. Inset: Fit of the pressure profile with the chain minimization method for $s = 0.55$. Curves are ordered from flat to peaked with increasing R on the left and in the inset, and from wide to narrow on the right.

F. Robustness and scaling of the band pattern

The band pattern explored in Secs. III A through III D is remarkably robust against perturbations and the central result of our continuum model, Eq. (21), has a wide range of validity. The band structure is the simplest topologically allowed state and can only be destroyed by a select number of effects. First, if the noise strength is too high, the alignment between particles disappears, and with it the polar order pattern, both in the flat case and on the sphere in what is essentially a Vicsek transition, translated to our model. Second, if the velocity is too low or if the alignment strength J is too low, the system explores states with different topologies. These include moving patches with a single defect and complex states with a dynamically folding band. These very intriguing new states will be explored in detail elsewhere [44].

We first explore the influence of system size. From our analytical results, Eq. (21), we see that the radius R enters only through the curvature $\kappa = 2\sigma/R$ and indirectly through the value of the band edge angle ϑ_m determined using the value of the parameter $\alpha \sim R$ from (B15) in (B14). In Fig. 10, we show the pressure profiles [Fig. 10(a)] and the $\alpha - \theta$ profiles [Fig. 10(b)] for a range of radii, $R = 8$ to $R = 60$, equivalent to almost two decades in system size N. Snapshots of a $R = 5$ and a $R = 60$ system can be seen in Fig. 11(a) and 11(b). It becomes clear that the reverse alignment parameter s is independent of R: It is a function of J only, with the universal value $s = 0.45$ for $J = 1$ [compare to Fig. 6(b)]. The band narrows with R (i.e., the edge angle decreases; the physical width does increase), and the peak pressure increases, consistent with the predictions of Eq. (21). As before, the general nonlinear elasticity introduced by double overlaps makes a quantitative comparison difficult; we rely on the chain energy minimization instead. In Fig. 10(b) (inset) we show the fitted values for the pressure profile at $s = 0.55$, the same value used above for $J = 1$, showing good agreement. The edge pressure $p = -\frac{v_0}{\sigma \mu}\sin(s\theta_m)$ depends on curvature only through the location of the band edge; our observed values barely depend on R, both in the simulation and the chain minimization fit. Consistent with the narrowing of the band, the order parameter increases with radius [Fig. 12(a), inset].

As a function of noise, we expect to see the disappearance of the band in the curved analog of the Vicsek transition. In Fig. 11(c) through 11(f), we show snapshots of the system with increasing noise strength. An invaluable tool to determine the motion pattern on the sphere is the tracking of defects in both the velocity and order parameter field (to be explored in more detail elsewhere [44]). All the examples above except Fig. 11(f) have a band-type location of defects; that is, two $+1$ defects each in both the velocity and order parameter field at opposite poles, with the locations of these defects for the two fields close to or identical to each other. The snapshot at the highest noise has a larger number of defects, consistent with a pattern where opposite-sign defect pairs nucleate in regions where the order breaks down. In Fig. 12(b), we show the number of defects in both fields as a function of noise strength. At low noise amplitudes, we observe two defects in each field (dotted line). The velocity field (especially at the lower $v_0 = 0.1\sigma/\tau$) is the first to nucleate defect pairs, followed by the order parameter field around $v_r = 2\tau^{-1}$. We then see a rapid transition to a
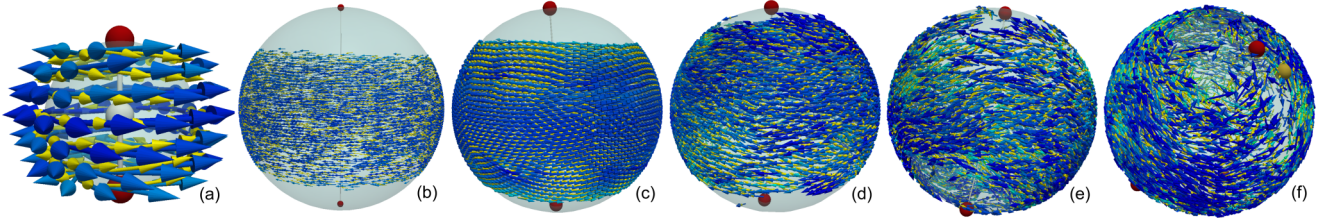
FIG. 11. (Color online) Evolution of the band as a function of radius and noise strength; all snapshots for $v_0 = 0.5\sigma/\tau$, $J = 1\tau^{-1}$ and $\phi = 1$. From left to right: bands for $R = 5\sigma$ and $R = 60\sigma$ for low noise strength $\nu_r = 0.002\tau^{-1}$, followed by bands at $R = 28.2\sigma$ and noise strength increasing from $\nu_r = 0$, $\nu_r = 0.3\tau^{-1}$ to $\nu_r = 1.0\tau^{-1}$ and through the transition to $\nu_r = 2\tau^{-1}$. Velocity is blue (dark), and the polar vector is colored yellow (light). The location of the velocity defects (red) and order parameter defects (yellow) is indicated by colored spheres; all snapshots except the highest noise one are topologically a band structure.

completely disordered system with dozens of defects (note the logarithmic scale on the y axis).

The order parameter $p_S = \frac{1}{NRv_0} \left| \sum_i \mathbf{r}_i \times \mathbf{v}_i \right|$ is another useful tool to track the disappearence of the band. It decreases nearly linearly as a function of ν_r, as can be seen in Fig. 12(a), and has overall smaller values for lower v_0 (consistent with a broader band). This is quite unlike the first-order transition observed in the original Vicsek model [24], or even a second-order transition, and indicates a more complex process. For example, at $\nu_r = 2\tau^{-1}$, where we begin nucleating defect pairs, the order parameter is still quite substantial $p_s \approx 0.6$, and we can also see substantial remaining local alignment in Fig. 11(f). The band has long been destroyed by the time the order parameter finally reaches 0, at $\nu_r \approx 5\tau^{-1}$.

While the band is still present, we can again investigate pressure and α profiles, shown in Figs. 13(a) and 13(b). The band broadens systematically with noise strength and the pressure eventually becomes homogeneous. Partially, we can explain this effect through the $\alpha - \theta$ relation shown in Fig. 13(b). From a value $s = 0.45$ at the lowest noise value, s decreases with noise and the fluctuations in the profile increase, until we eventually recover a homogeneous system. Here s is then a measure of the alignment strength of $\mathbf{n}_i$ with the band geometry, opposite its role as a reverse alignment strength as

a function of J. The full situation is more complex, though: For all but the lowest noise value, the clearly defined pressure jump at the band edge disappears. This indicates that we lose a distinct band edge due to inward pressing particles stuck at the interface; we can also see particles invading the bald spot in Figs. 11(d) and 11(e). Again, this situation is reminiscient of the mechanism of phase separation in nonaligning soft active particles [26,27], where the phase separation disappears at sufficiently low Péclet numbers $Pe = v_0/\sigma\nu_r$. At the low noise strengths investigated in the main part of this paper, we have $Pe = 250$, well in the phase-separated regime, and our order-disorder transition here occurs around $Pe = 1$. At these highest noise strengths, we also observe an overall active contribution to the pressure $p \approx 0.8$, well above the $p_0 \approx 0.6$ due to only the passive overlaps.

IV. SUMMARY AND CONCLUSIONS

In this paper we have constructed a model of soft spherical active particles confined to move on the surface of a sphere. Our goal was to devise the simplest possible nontrivial model that would allow us to identify and characterize the effects of curvature and topology on active motion. Using numerical simulations and analytical arguments we have shown that activity and curvature combine to produce interesting types of active patterns: a polar vortex and a stable rotating-band structure. These states are purely consequence of nontrivial topology and do not have simple planar counterparts.
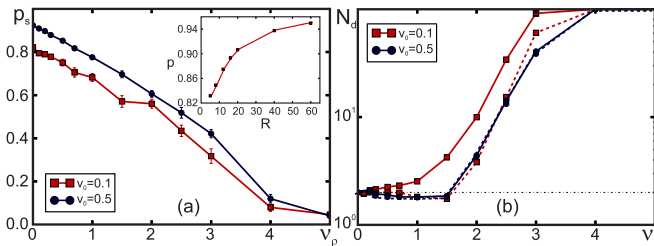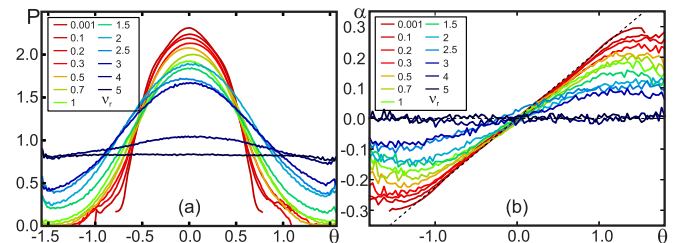

FIG. 12. (Color online) (a) Order parameter as a function of noise strength and velocity v_0. The order linearly decreases with noise, but with no sign of a clear order-disorder transition. For the lowest v_0, more complex band folding dynamics can be observed at low noise strengths, to be explored in detail elsewhere [44]. Inset: Order parameter as a function of radius. (b) Number of defects of the velocity field (solid) and the order parameter field (dashed) as a function of noise strength and velocity. From a value of 2 corresponding to the band state, first the velocity field and finally the order parameter field nucleate defect pairs until the band pattern abruptly disappears around $\nu_r = 2.5\tau^{-1}$.

FIG. 13. (Color online) Scaling of the band properties with noise strength σ. Left: Pressure profiles starting from low noise levels (red), crossing through the transition around $\nu_r = 3\tau^{-1}$, until the system becomes homogeneous at $\nu_r = 5\tau^{-1}$, for $v_0 = 0.5\sigma/R$, $\phi = 1$ and $J = 1\tau^{-1}$. Right: The $\alpha = s\theta$ relation is still valid, however $s(\nu_r)$ decreases systematically; the dashed line is $s = 0.45$. Curves are ordered from peaked to flat with increasing ν_r on the left, and from steep to shallow on the right.

Here, for simplicity, we have only focused on overdamped polar active particles and neglected all hydrodynamic effects. However, we retained steric effects in order to prevent collapse into a trivial linelike equatorial ring state if steric repulsion were absent.

Many open questions still remain to be answered. In particular, the nonzero Gaussian curvature of the underlaying surface induces topological defects in the vector fields attached to it (e.g., velocity or particle direction), and these can be used to classify the dynamical structures observed, as we showed with the order-disorder transition. We have tracked defects, but we still have to fully explore the wealth of curvature-induced active states, especially in the low-activity regime, where we observe misalignment between defects in the **v** and **n** fields. It will be intriguing to develop an understanding of the interplay between elasticity and driving in the dynamics of these topological defects. The sphere is special for its uniform curvature. At present nothing is known about how varying curvature would affect motion patterns. Would the flock move along the path with the lowest curvature or maybe along geodesics? What happens if the system is dilute and active phase separation prevents the elongated band states from forming? What happens if we change the internal symmetry of the active agents, e.g., from polar to nematic? Finally, what would be the effects of hydrodynamic interactions? A full description and understanding of the recent experiment nematic active systems on a droplet [42] would likely require addressing hydrodynamic effects in detail. This would ultimately require generalizing hydrodynamic descriptions of active systems [2] to curved spaces, which is both conceptually and technically a formidable task. Some of these question will be addressed in the subsequent publications.

We hope that this work will stimulate further research in this largely unexplored field with possible experimental realizations (e.g., by using self-propelled colloids on droplets). It will also potentially have considerable applications in cell and developmental biology, especially concerning the motion of epithelial cell sheets on curved substrates such as the intestine or the cornea.

APPENDIX A: CONSTRAINED MOTION ON A SPHERE

In this Appendix we derive the equations for active, self-propelled constrained motion on a sphere. The theoretical basis for the treatment presented here can be found, e.g., in Ref. [51]. Consider the following full set of Newtonian equations of motion in three dimensions for the spatial variables $\mathbf{r}_i$

$$m\ddot{\mathbf{r}}_i = -\gamma\dot{\mathbf{r}}_i + \sum_j \mathbf{F}_{ij} + \mathbf{F}_i^{\text{act}}, \qquad \text{(A1)}$$

where the active force $\mathbf{F}_i^{\text{act}}$ is treated as an independent parameter.

In standard Hamiltonian dynamics, holonomic constraints do not depend on the generalized velocities $\dot{q}_i$ and can be expressed as a function of the generalized coordinates q_i only. If such a constraint α is written as an equation $g_\alpha(\mathbf{q}) = \mathbf{0}$ ($\mathbf{q} = \{q_1, \ldots, q_N\}$, where N_{tot} is the total number of degrees of freedom), $g_\alpha(\mathbf{q})$ can be interpreted as a potential, and the constraint trajectories will then lie on the isopotential surface with potential value 0. The spherical constraint $g(\mathbf{r}) = x^2 + y^2 + z^2 - R^2$ is a classic example of such a constraint. A reasoning similar to electrostatics or gravitation leads to the result that the constraint forces keeping the system on its isopotential surface need to be normal to this surface. In other words, they must be along the gradient of g, so for each constraint there exists a constraint force $\mathbf{F}_\alpha = \lambda_\alpha \nabla_{\mathbf{q}} g_\alpha(\mathbf{q})$ that penalizes any deviations from the isopotential surface.

Then for a set of constraints $\{g_\alpha(\mathbf{q}) = 0 | \alpha = 1, \ldots, M\}$, and an explicitly Hamiltonian system, the equations of motion are [51]

$$\frac{d\mathbf{q}}{dt} = \mathbf{v}$$
$$m\frac{d\mathbf{v}}{dt} = -\nabla_{\mathbf{q}} V(\mathbf{q}) - \sum_\alpha \lambda_\alpha \nabla_{\mathbf{q}} g_\alpha(\mathbf{q}). \qquad \text{(A2)}$$

To determine the multipliers λ_α, we can take further derivatives of the constraint equations:

$$\frac{d}{dt}(g_\alpha(\mathbf{q})) = \nabla_{\mathbf{q}} g_\alpha(\mathbf{q}) \cdot \mathbf{v} = 0. \qquad \text{(A3)}$$

As to be expected, this shows that $\mathbf{v}$ belongs to the tangent bundle of the constraint surface $g_\alpha(\mathbf{q})$. Finally, to determine λ_α, we can differentiate this equation once more and then substitute the equations of motion, Eq. (A2). We should then obtain a set of M equations to determine the M multipliers λ_α. Depending on our choice of constraints, these equations will be linearly independent and offer a unique set of λ_α.

Even though the active part of Eq. (A1) does not derive from a potential, the steps outlined above remain valid. We choose the set of positions $\{\mathbf{r}_i\} \equiv \mathbf{q}$ as generalized coordinates. The gradient of our constraint $g(\mathbf{r}_i) = x_i^2 + y_i^2 + z_i^2 - R^2$ is $\nabla_{\mathbf{r}_i} g(\mathbf{r}_i) = 2\mathbf{r}_i$. Then the constraint equations of motion become

$$m\ddot{\mathbf{r}}_i = -\gamma\dot{\mathbf{r}}_i + \sum_j \mathbf{F}_{ij} + \mathbf{F}_i^{\text{act}} - 2\lambda_i \mathbf{r}_i. \qquad \text{(A4)}$$

Note that the constraint applies to each particle independently and, thus, λ has index i. The derivative constraint just leads to the equation $\dot{\mathbf{r}}_i \cdot \mathbf{r}_i = 0$. If we define the unit normal to the sphere as $\hat{\mathbf{r}}_i = \mathbf{r}_i / |\mathbf{r}_i| = \mathbf{r}_i / R$, this confirms that the velocity has to be tangential to the surface of the sphere.

The constraint due to the second derivative finally allows us to determine λ_i, and after substituting Eq. (A4) we obtain:

$$2\lambda_i = \frac{1}{r_i^2}\left[mv_i^2 + \mathbf{r}_i \cdot \left(\mathbf{F}_i^{\text{act}} + \sum_j \mathbf{F}_{ij}\right)\right]. \qquad \text{(A5)}$$

Then, after substituting λ_i back into Eq. (A4), we can write equations of motion that fully implement the spherical

constraint:

$$m\ddot{\mathbf{r}}_i = -\gamma \dot{\mathbf{r}}_i + \sum_j \mathbf{F}_{ij} + \mathbf{F}_i^{\text{act}}$$

$$-\frac{\mathbf{r}_i}{r_i^2}\left[m\dot{r}_i^2 + \mathbf{r}_i \cdot \left(\mathbf{F}_i^{\text{act}} + \sum_j \mathbf{F}_{ij} \right) \right]. \quad \text{(A6)}$$

In the overdamped limit, we can see that $m \to 0$ does not produce any singularities and we can write the valid equations of motion:

$$\gamma \dot{\mathbf{r}}_i = \mathbf{F}_i^{\text{act}} - \left(\hat{\mathbf{r}}_i \cdot \mathbf{F}_i^{\text{act}} \right)\mathbf{r}_i + \sum_j \mathbf{F}_{ij} - (\hat{\mathbf{r}}_i \cdot \mathbf{F}_{ij})\mathbf{r}_i. \quad \text{(A7)}$$

APPENDIX B: EULERIAN VERSUS LAGRANGIAN PICTURES

In this Appendix we derive continuum equations for a rotating elastic chain on a sphere subject to active forces (Fig. 5), using Eulerian and Lagrangian pictures, starting from Eq. (8). Let ϑ be the underlying angular coordinate we would like to use for our solutions, with $\vartheta = 0$ at the equator. Since we use an absolute coordinate system, and not the particles themselves for coordinates, this approach is in the Eulerian picture [52]. Conversely, if we use the original positions of the particles, θ_0, as a reference, the approach is Lagrangian. Habitually, Eulerian and Lagrangian elasticity are defined as follows. Let R be the original positions in the undistorted material. Then, after distortion, their coordinates are given by $x(R) = R + u(R)$, where the initial positions R are used as reference frame. Lagrangian elasticity is based on this approach: Distances in the distorted material are expressed as $dx^2 - dR^2 = 2u_{ij}^L(R)dR_i dR_j$ (assuming the Einstein summation convention), where $u_{ij}^L(R)$ is the Lagrangian strain tensor,

$$u_{ij}^L(R) = \frac{1}{2}\left[\frac{\partial u_i}{\partial R_j} + \frac{\partial u_j}{\partial R_i} + \frac{\partial u_k}{\partial R_i}\frac{\partial u_k}{\partial R_j} \right]. \quad \text{(B1)}$$

In a Eulerian approach, we use the new coordinates x in the absolute reference frame as a basis, and we have to invert the relation above to have $R(x) = x - u(R(x))$, which then leads to the Eulerian strain tensor $dx^2 - dR^2 = 2u_{ij}^E(x)dx_i dx_j$. The Eulerian strain tensor therefore has a minus sign in the nonlinear term, opposite to the more familiar Lagrangian strain tensor:

$$u_{ij}^E(x) = \frac{1}{2}\left[\frac{\partial u_i}{\partial x_j} + \frac{\partial u_j}{\partial x_i} - \frac{\partial u_k}{\partial x_i}\frac{\partial u_k}{\partial x_j} \right]. \quad \text{(B2)}$$

For us, the initial relation $x(R) = R + u(R)$ is simply $\vartheta = \theta_i = \theta_{i,0} + u_i$, which we then need to invert to obtain $R(x) = x - u(R(x))$, i.e., $\theta_{i,0}(\vartheta) = \vartheta - u(\theta_{i,0}(\vartheta))$. The strain tensor is affected by the one-dimensional nature of our problem. By definition, the metric tensor has to be a perfect square for a one-dimensional problem, $dx^2 = g^L(R)dR^2$, so $g^L(R) = (1 + du/dR)^2$ and $dR^2 = g^E(x)dx^2$ with $g^E(x) = (1 - du/dx)^2$.

In our coordinates, we then derive the strain tensors:

$$u_s^L = \frac{du}{d\theta^0} + \frac{1}{2}\left(\frac{du}{d\theta_0} \right)^2, \quad \text{(B3)}$$

$$u_s^E = \frac{du}{d\vartheta} - \frac{1}{2}\left(\frac{du}{d\vartheta} \right)^2. \quad \text{(B4)}$$

To recover the underlying periodicity of the chain (the i index), recall the standard definition of a reciprocal vector G for a lattice: $GR = 2\pi m$, where m is an integer. For us $G\theta_{i,0} = 2\pi i$. In the ϑ basis, the old positions of the undistorted lattice points still have to follow $G(x - u(x)) = 2\pi m$, that is, for us then $G[\vartheta - u(\vartheta)] = 2\pi i$, or, using the lattice definition of the $\theta_{i,0}$, $\theta_{i,0}(\vartheta) = \vartheta - u(\vartheta) = \frac{2\sigma i}{R} - \frac{\sigma N}{R}$.

For the Lagrangian coordinates, the transformation to continuum is then straightforward: We can approximate the angle differences as $\theta_i - \theta_{i-1} = \theta_{i,0} - \theta_{i-1,0} + u(\theta_{i,0}) - u(\theta_{i-1,0}) \approx \frac{2\sigma}{R} + \frac{2\sigma}{R}\frac{du}{d\theta_0}$. The double angle difference $\theta_{i+1} + \theta_{i-1} - 2\theta_i = \theta_{i+1,0} - \theta_{i-1,0} - 2\theta_{i,0} + u(\theta_{i+1,0}) + u(\theta_{i-1,0}) - 2u(\theta_{i,0}) \approx [\frac{2\sigma}{R}]^2 \frac{d^2u}{d\theta_0^2}$ becomes now clearly a discrete Laplacian. In Eulerian coordinates, the complexity arises from the difference in line element inherent in passing to the new coordinates ϑ. Though we clearly have above $d\theta_0 = \theta_{i,0} - \theta_{i-1,0} = 2\sigma/R$, in the new coordinates we need to express it as a function of the new line element $d\vartheta$, $d\theta_0 = \sqrt{g^E}d\vartheta$, or, more explicitly, $d\vartheta = (1 + \frac{du}{d\vartheta})d\theta_0(\vartheta)$. Then the angle differences become $\theta_i - \theta_{i-1} \approx \frac{2\sigma}{R} + \frac{2\sigma}{R}(1 + \frac{du}{d\vartheta})\frac{du}{d\vartheta}$ and $\theta_{i+1} + \theta_{i-1} - 2\theta_i \approx [\frac{2\sigma}{R}]^2(1 + \frac{du}{d\vartheta})^2 \frac{d^2u}{d\vartheta^2}$, a much more complex set of derivatives.

Finally, in Eq. (8), the resultant force in the polar direction resulting from the active motion still acts at the *distorted* points θ_i. We can formally write $\theta_i = \theta_{i,0}(\vartheta) + u(\theta_{i,0}(\vartheta))$ in Eulerian coordinates to see just as quickly that we get $\theta_i = \vartheta - u(\theta_{i,0}(\vartheta)) + u(\theta_{i,0}(\vartheta)) = \vartheta$, simply the angular coordinate. This makes sense since the active Coriolis force is solely due to the constrained motion in the curved reference frame and completely independent of the initial particle positions. In the Lagrangian frame, we need to keep track of the displacements from the origin: $\theta_i = \theta_{i,0} + u(\theta_{i,0})$. The active force contribution becomes tractable if we use the results from Fig. 6 and assume that $\alpha = s\vartheta$ or, equivalently, $\alpha = s\theta_0 + su$. In the Lagrangian reference frame, we have the equations

$$\frac{d^2u}{d\theta_0^2} = \alpha \sin(s\theta_0 + su), \quad \text{(B5)}$$

with boundary conditions

$$\left. \frac{du}{d\theta_0} \right|_{-\theta_{m,0}} = \beta \sin(s\theta_0 + su)$$

$$\left. \frac{du}{d\theta_0} \right|_{\theta_{m,0}} = -\beta \sin(s\theta_0 + su). \quad \text{(B6)}$$

In the Eulerian reference frame, the right-hand side term is simpler; however, additional derivatives arise on the left-hand side:

$$\left(1 + \frac{du}{d\vartheta}\right)^2 \frac{d^2u}{d\vartheta^2} = \alpha \sin(s\vartheta), \quad \text{(B7)}$$

with boundary conditions

$$\left(1 + \frac{du}{d\vartheta}\right)\frac{du}{d\vartheta}\bigg|_{-\vartheta_m} = \beta \sin(s\vartheta)$$

$$\left(1 + \frac{du}{d\vartheta}\right)\frac{du}{d\vartheta}\bigg|_{\vartheta_m} = -\beta \sin(s\vartheta). \tag{B8}$$

Here $\alpha = \frac{1}{R}\left[\frac{R}{2\sigma}\right]^2 \frac{v_0}{\mu k}$ and $\beta = \frac{v_0}{2\sigma\mu k}$, and the boundary conditions have to be taken at the original position of the chain edges $\theta_{m,0}$ in the Lagrangian case, but at the final position ϑ_m for the Eulerian equations.

Neither of Eqs. (B5) and (B7), unfortunately, has an analytical solution. In Fig. 9, we compare the approximate results to the discrete energy minimization approach for the chain and show that they are valid in the low-v_0 regime. In both the Lagrangian and Eulerian cases, the zeroth-order equation that can be solved is

$$\frac{d^2u}{d\theta^2} = \alpha \sin(s\theta), \tag{B9}$$

with boundary condition

$$\frac{du}{d\theta}\bigg|_{\theta_m} = -\beta \sin(s\theta_m) \tag{B10}$$

and equivalently at $-\theta_m$. The solution to this equation is

$$u(\theta) = -\alpha/s^2 \sin s\theta + c\theta + d, \tag{B11}$$

where c and d are integration constants. We can immediately see that the symmetries $u(-\theta) = -u(\theta)$ and $u(0) = 0$ require that $d = 0$. Clearly, the two boundary conditions are equivalent, and we are left with $-\alpha/s \cos s\theta_m + c = -\beta \sin s\theta_m$ to determine c.

We still lack a relation tying θ_m to the underlying physics of the chain. In the Lagrangian case, $\theta_{m,0}$ is simply the initial extent of the chain before the active forces are applied. Since at our high density, the sphere is covered in particles in the absence of driving, we can safely assume $\theta_{m,0} = \pi/2$. In the Eulerian case, this is slightly more tricky. Consider the elementary differential geometry relation for a curve $\mathcal{C}$ parametrized by $\mathbf{l}(t)$ in space S. Its length is given by $L = \int_\mathcal{C} \sqrt{\sum_k (dl_k/dt)^2} dt$ [53]. In our Eulerian approach, $\vartheta = t$, the parametrization, and the mapped space S belongs to the original $\theta_0 = \mathbf{l}$, and $L = \pi$ is the original length of the chain. If this seems backwards, it is compared to a more standard Lagrangian parametrization, where it would be the other way round. The set of derivatives are now simply the square root of the metric tensor, $d\theta_0/d\vartheta = (1 - du/d\vartheta) = \sqrt{g^E(\vartheta)}$. Then the missing equation linking the original chain length and the displacement field is

$$\pi = \int_{-\vartheta_m}^{\vartheta_m} d\vartheta \left(1 - \frac{du}{d\vartheta}\right). \tag{B12}$$

This last equation does not have an analytical solution, and the approximate solution to the chain profile in Eulerian coordinates can only be given implicitly:

$$u(\vartheta) = -\alpha/s^2 \sin s\vartheta + (\alpha/s \cos s\vartheta_m - \beta \sin s\vartheta_m)\vartheta, \tag{B13}$$

$$\pi = \frac{2\alpha}{s^2} \sin(s\vartheta_m) + 2\theta_m \left[1 - \alpha/s \cos(s\vartheta_m) + \beta \sin(s\vartheta_m)\right], \tag{B14}$$

$$\alpha = \frac{1}{R}\left[\frac{R}{2\sigma}\right]^2 \frac{v_0}{\mu k}, \quad \beta = \frac{v_0}{2\sigma\mu k}. \tag{B15}$$

[1] T. Vicsek and A. Zafeiris, Phys. Rep. **517**, 71 (2012).
[2] M. Marchetti, J. Joanny, S. Ramaswamy, T. Liverpool, J. Prost, M. Rao, and R. A. Simha, Rev. Mod. Phys. **85**, 1143 (2013).
[3] A. Sokolov, I. S. Aranson, J. O. Kessler, and R. E. Goldstein, Phys. Rev. Lett. **98**, 158102 (2007).
[4] B. Szabó, G. J. Szöllösi, B. Gönci, Z. Jurányi, D. Selmeczi, and T. Vicsek, Phys. Rev. E **74**, 061908 (2006).
[5] F. Jülicher, K. Kruse, J. Prost, and J.-F. Joanny, Phys. Rep. **449**, 3 (2007).
[6] C. K. Hemelrijk and H. Kunz, Behav. Ecol. **16**, 178 (2005).
[7] I. L. Bajec and F. H. Heppner, Anim. Behav. **78**, 777 (2009).
[8] I. R. Fischhoff, S. R. Sundaresan, J. Cordingley, H. M. Larkin, M.-J. Sellier, and D. I. Rubenstein, Anim. Behav. **73**, 825 (2007).
[9] L. Giomi, M. J. Bowick, X. Ma, and M. C. Marchetti, Phys. Rev. Lett. **110**, 228101 (2013).
[10] S. P. Thampi, R. Golestanian, and J. M. Yeomans, Europhys. Lett. **105**, 18001 (2014).
[11] J. Palacci, S. Sacanna, A. P. Steinberg, D. J. Pine, and P. M. Chaikin, Science **339**, 936 (2013).
[12] J. Deseigne, O. Dauchot, and H. Chaté, Phys. Rev. Lett. **105**, 098001 (2010).
[13] D. Helbing, Rev. Mod. Phys. **73**, 1067 (2001).

[14] B. Vasiev, A. Balter, M. Chaplain, J. A. Glazier, and C. J. Weijer, PLoS ONE **5**, e10571 (2010).
[15] A. Fatehullah, P. L. Appleton, and I. S. Näthke, Philos. Trans. R. Soc. B: Biol. Sci. **368**, 20130014 (2013).
[16] L. Ritsma, S. I. Ellenbroek, A. Zomer, H. J. Snippert, F. J. de Sauvage, B. D. Simons, H. Clevers, and J. van Rheenen, Nature **507**, 362 (2014).
[17] J. M. Collinson, L. Morris, A. I. Reid, T. Ramaesh, M. A. Keighren, J. H. Flockhart, R. E. Hill, S.-S. Tan, K. Ramaesh, B. Dhillon, and J. D. West, Dev. Dyn. **224**, 432 (2002).
[18] T. Sanchez, D. T. Chen, S. J. DeCamp, M. Heymann, and Z. Dogić, Nature **491**, 431 (2012).
[19] T. Vicsek, A. Czirók, E. Ben-Jacob, I. Cohen, and O. Shochet, Phys. Rev. Lett. **75**, 1226 (1995).
[20] N. D. Mermin and H. Wagner, Phys. Rev. Lett. **17**, 1133 (1966).
[21] J. Toner and Y. Tu, Phys. Rev. Lett. **75**, 4326 (1995).
[22] E. Bertin, M. Droz, and G. Grégoire, Phys. Rev. E **74**, 022101 (2006).
[23] T. Ihle, Phys. Rev. E **83**, 030901 (2011).
[24] H. Chaté, F. Ginelli, G. Grégoire, and F. Raynaud, Phys. Rev. E **77**, 046113 (2008).
[25] S. Henkes, Y. Fily, and M. C. Marchetti, Phys. Rev. E **84**, 040301 (2011).

[26] J. Tailleur and M. E. Cates, Phys. Rev. Lett. **100**, 218103 (2008).

[27] Y. Fily and M. C. Marchetti, Phys. Rev. Lett. **108**, 235702 (2012).

[28] J. Bialké, T. Speck, and H. Löwen, Phys. Rev. Lett. **108**, 168301 (2012).

[29] L. Berthier and J. Kurchan, Nat. Phys. **9**, 310 (2013).

[30] P. Romanczuk, M. Bär, W. Ebeling, B. Lindner, and L. Schimansky-Geier, Eur. Phys. J. Spec. Top. **202**, 1 (2012).

[31] Y. Fily, A. Baskaran, and M. F. Hagan, Soft Matter **10**, 5609 (2014).

[32] J. Stenhammar, D. Marenduzzo, R. J. Allen, and M. E. Cates, Soft Matter **10**, 1489 (2014).

[33] Y. Fily, S. Henkes, and M. C. Marchetti, Soft Matter **10**, 2132 (2014).

[34] G. S. Redner, M. F. Hagan, and A. Baskaran, Phys. Rev. Lett. **110**, 055701 (2013).

[35] M. R. D'Orsogna, Y. L. Chuang, A. L. Bertozzi, and L. S. Chayes, Phys. Rev. Lett. **96**, 104302 (2006).

[36] J. Strefler, U. Erdmann, and L. Schimansky-Geier, Phys. Rev. E **78**, 031927 (2008).

[37] A. Bausch, M. Bowick, A. Cacciuto, A. Dinsmore, M. Hsu, D. Nelson, M. Nikolaides, A. Travesset, and D. Weitz, Science **299**, 1716 (2003).

[38] W. T. Irvine, V. Vitelli, and P. M. Chaikin, Nature **468**, 947 (2010).

[39] M. J. Bowick, D. R. Nelson, and A. Travesset, Phys. Rev. B **62**, 8738 (2000).

[40] W. T. Irvine and V. Vitelli, Soft Matter **8**, 10123 (2012).

[41] M. Do Carmo, *Differential Geometry of Curves and Surfaces*, Vol. 1 (Prentice-Hall, Englewood Cliffs, NJ, 1976).

[42] F. C. Keber, E. Loiseau, T. Sanchez, S. J. DeCamp, L. Giomi, M. J. Bowick, M. C. Marchetti, Z. Dogic, and A. R. Bausch, Science **345**, 1135 (2014).

[43] See Supplemental Material at http://link.aps.org/supplemental/10.1103/PhysRevE.91.022306 for movies of the motion patterns.

[44] S. Henkes and R. Sknepnek (unpublished).

[45] P. Srivastava, R. Shlomovitz, N. S. Gov, and M. Rao, Phys. Rev. Lett. **110**, 168104 (2013).

[46] G. Grégoire and H. Chaté, Phys. Rev. Lett. **92**, 025702 (2004).

[47] C. Zhu, R. H. Byrd, P. Lu, and J. Nocedal, ACM Trans. Math. Software (TOMS) **23**, 550 (1997).

[48] C. S. O'Hern, L. E. Silbert, A. J. Liu, and S. R. Nagel, Phys. Rev. E **68**, 011306 (2003).

[49] R. C. Ball and R. Blumenfeld, Phys. Rev. Lett. **88**, 115505 (2002).

[50] J. H. Irving and J. G. Kirkwood, J. Chem. Phys. **18**, 817 (1950).

[51] B. Leimkuhler and S. Reich, *Simulating Hamiltonian Dynamics* (Cambridge University Press, Cambridge, UK, 2004).

[52] P. Chaikin and T. Lubensky, *Principles of Condensed Matter Physics* (Cambridge University Press, Cambridge, UK, 2000).

[53] J. Schmets, *Analyse Mathematique* (Editions Derouaux, Liege, Belgium, 1994).